

Photocatalytic H<sub>2</sub> evolution on graphdiyne/g-C<sub>3</sub>N<sub>4</sub> hybrid nanocompositesQuanlong Xu<sup>a,d</sup>, Bicheng Zhu<sup>a</sup>, Bei Cheng<sup>a</sup>, Jiaguo Yu<sup>a,\*</sup>, Minghua Zhou<sup>b,\*</sup>, Wingkei Ho<sup>c,\*</sup><sup>a</sup> State Key Laboratory of Advanced Technology for Materials Synthesis and Processing, Wuhan University of Technology, Wuhan, 430070, PR China<sup>b</sup> Hubei Key Laboratory of Wudang Local Chinese Medicine Research, Hubei University of Medicine, Shiyan, 442000, PR China<sup>c</sup> Department of Science and Environmental Studies and State Key Laboratory in Marine Pollution, The Hong Kong Education University of Hong Kong, Tai Po, N. T. Hong Kong, PR China<sup>d</sup> Zhejiang Key Laboratory of Carbon Materials, Wenzhou University, Wenzhou 325027, PR China

## ARTICLE INFO

## Keywords:

g-C<sub>3</sub>N<sub>4</sub>/graphdiyne  
Hydrogen generation  
Photocatalysis

## ABSTRACT

Hydrogen is considered an ideal alternative energy source to replace fossil energy. Herein, a novel graphdiyne (GD)/graphitic carbon nitride (g-C<sub>3</sub>N<sub>4</sub>) nanocomposite was successfully synthesized via a facile calcination approach, and display excellent H<sub>2</sub>-generation performance under visible light. When the mass ratio of GD reaches 0.5 wt% in GD/g-C<sub>3</sub>N<sub>4</sub> nanocomposite, it shows a maximum hydrogen evolution rate, exceeding that of g-C<sub>3</sub>N<sub>4</sub> by 6.7-fold. After systematic characterization, a new C–N bond is confirmed to form between GD and g-C<sub>3</sub>N<sub>4</sub> following heat treatment, and this bond serves as a charge carrier channel that facilitates the migration of photogenerated electrons from g-C<sub>3</sub>N<sub>4</sub> to GD. Positive effects, such as a prolonged photogenerated charge carrier lifetime, intensified electron density, decreased reaction overpotential and improved charge carrier mobility, also contribute to the enhanced photocatalytic performance of the nanocomposites. The proposed technique provides a promising approach for modifying photocatalysts in future applications.

## 1. Introduction

Photocatalytic hydrogen (H<sub>2</sub>) evolution, a water splitting half-reaction, has attracted great attention for its ability to convert solar to chemical energy and the merits of H<sub>2</sub>, which include high density and a water-only combustion product. The development of a suitable semiconductor photocatalyst is crucial for this half-reaction, as this photocatalyst must not only satisfy the band level requirement for water splitting but should also be efficient, robust and inexpensive [1]. Although an abundance of semiconductor photocatalysts, such as metal oxide-, sulphide- and nitride-based semiconductors, have been explored by several researchers to catalyze this highly desirable reaction, satisfying practical energy conversion efficiency requirements remains challenging [2–5]. The existing shortcomings, which include a large overpotential, wide band gap, fast recombination of photogenerated charge carriers and rapid photo-corrosion, limit the performance of the available photocatalysts. In this regard, polymeric photocatalysts have aroused great interest and are considered promising candidates because of their easily tailorable electronic structure and tunable optical absorption properties [6–9].

As a typical polymeric photocatalyst, g-C<sub>3</sub>N<sub>4</sub> was first applied to the photocatalytic water-splitting reaction to generate H<sub>2</sub> in 2009 [10]; since then, numerous works have been conducted to investigate its

photocatalytic performance, and remarkable accomplishments have been achieved [11–17]. Due to its repeating  $\pi$ -conjugated heptazine ring units hybridized with sp<sup>2</sup> carbon and nitrogen in plane, g-C<sub>3</sub>N<sub>4</sub> presents superior physicochemical properties and a unique electronic structure. However, because of the weak van der Waals force between adjacent layers, g-C<sub>3</sub>N<sub>4</sub> suffers from weak electron coupling between layers. In addition, the photogenerated electron–hole pairs of g-C<sub>3</sub>N<sub>4</sub> are easily recombined. These disadvantages endow g-C<sub>3</sub>N<sub>4</sub> with low photocatalytic activity [11,18–22]. Significant improvements in photocatalytic performance have been achieved by g-C<sub>3</sub>N<sub>4</sub> modification through morphology control [23,24], copolymerization [25], doping [26–29], and combination with other materials [15,30–37]. Carbonaceous materials rich in  $\pi$ -conjugated skeletons are believed to be a promising material for coupling with g-C<sub>3</sub>N<sub>4</sub> to improve its photocatalytic activity [38,39].

Indeed, some carbonaceous materials exhibit significant positive effects on improving the photocatalytic performance of g-C<sub>3</sub>N<sub>4</sub> [40]. Photo-induced electron–hole pairs can be efficiently separated after combination of metal-free carbonaceous materials with g-C<sub>3</sub>N<sub>4</sub> [41–43]. A new carbon allotrope, graphdiyne (GD), was recently developed; this material differs from common carbonaceous materials composed of extended networks with sp<sup>3</sup> and sp<sup>2</sup> hybridized carbon by featuring sp and sp<sup>2</sup> hybridized carbon atom networks in the form of

\* Corresponding authors.

E-mail addresses: [yujiaguo93@whut.edu.cn](mailto:yujiaguo93@whut.edu.cn) (J. Yu), [zmhsy2000@hbm.edu.cn](mailto:zmhsy2000@hbm.edu.cn) (M. Zhou), [keithho@ied.edu.hk](mailto:keithho@ied.edu.hk) (W. Ho).<https://doi.org/10.1016/j.apcatb.2019.117770>

Received 9 April 2019; Received in revised form 20 May 2019; Accepted 23 May 2019

Available online 25 May 2019

0926-3373/ © 2019 Elsevier B.V. All rights reserved.

benzene rings linked by diene units [44]. This unique structure endows GD with highly  $\pi$ -conjugated structure and excellent stability [45,46]. Due to its delocalized  $\pi$ -systems, GD shows a particularly excellent conductivity of  $2.5 \times 10^{-4} \text{ S m}^{-1}$  [34], and its intrinsic electron mobility is  $2 \times 10^5 \text{ cm}^2 \text{ V}^{-1} \text{ s}^{-1}$ , even higher than those of carbon nanotubes and graphene [47]. Considering these benefits, introduction of GD to semiconductor photocatalysts is expected to improve the photocatalytic performance of the latter to levels surpassing those of carbon nanotubes and graphene [48,49].

In the present work, GD was employed to modify g-C<sub>3</sub>N<sub>4</sub> and improve its photocatalytic water-splitting performance under visible light. GD/g-C<sub>3</sub>N<sub>4</sub> hybrids were obtained by annealing a homogenous mixture of GD and g-C<sub>3</sub>N<sub>4</sub>. A new C–N bond is formed between GD and g-C<sub>3</sub>N<sub>4</sub>, and this bond serves as the link through which the interaction between GD and g-C<sub>3</sub>N<sub>4</sub> is enhanced. Coupling g-C<sub>3</sub>N<sub>4</sub> with GD not only facilitates photogenerated charge carrier separation but also prolongs the charge carrier lifetime, intensifies the electron density, decreases the reaction overpotential and promotes electron mobility in the photocatalyst. These positive effects endow GD/g-C<sub>3</sub>N<sub>4</sub> hybrids with superior photocatalytic performance. In particular, application of 0.5 wt% GD to g-C<sub>3</sub>N<sub>4</sub> yields a maximum H<sub>2</sub> evolution rate of  $39.6 \mu\text{mol h}^{-1}$ , exceeding that of g-C<sub>3</sub>N<sub>4</sub> by 6.7-fold.

## 2. Experimental section

### 2.1. Sample preparation

Bulk g-C<sub>3</sub>N<sub>4</sub> was prepared by annealing 20 g of urea in the air at 550 °C for 2 h at a heating rate of  $5^\circ\text{C min}^{-1}$ . GD was synthesized according to a previous method [44]. Hexaethynylbenzene was used as the monomer and the cross-coupling reaction was conducted on a copper surface. To obtain the GD/g-C<sub>3</sub>N<sub>4</sub> composite, a calcination method was employed because of the high thermal resistance of GD [50]. In a typical process, a homogenous GD suspension was obtained by adding 5 mg of GD to 45 mL of methanol solution (66.7%) and sonication for 0.5 h, 200 mg of bulk g-C<sub>3</sub>N<sub>4</sub> was also suspended into 100 mL of water with sonication for 1 h. Subsequently, a certain amount of the GD solution was added to the bulk g-C<sub>3</sub>N<sub>4</sub> suspension under vigorous stirring for 1 h. After removal of the solvents, the resulting mixture was heat-treated at 400 °C for 2 h to obtain GD/g-C<sub>3</sub>N<sub>4</sub>. According to the different weight ratios of GD, the resulting GD/g-C<sub>3</sub>N<sub>4</sub> composites were denoted 0.25%GD/g-C<sub>3</sub>N<sub>4</sub>, 0.5%GD/g-C<sub>3</sub>N<sub>4</sub> and 1%GD/g-C<sub>3</sub>N<sub>4</sub>. For a fair comparison, g-C<sub>3</sub>N<sub>4</sub> was obtained through the same heat-treatment process without adding GD. A physical mixture of GD and g-C<sub>3</sub>N<sub>4</sub> was also prepared, and this sample was denoted Mix.

### 2.2. Characterization

The crystal structure of the photocatalysts was confirmed by X-ray diffraction (XRD), which was conducted on D/MAX-RB diffractometer (Rigaku, Japan) with CuK $\alpha$  radiation ( $\lambda = 1.5405 \text{ \AA}$ ). To investigate the morphology and microstructure of the samples, transmission electron microscopy (TEM) was performed on a Titan G<sup>2</sup> 60–300 instrument at a voltage of 300 kV. The surface composition and chemical states of the products were examined by X-ray photoelectron spectroscopy (XPS) using an ESCALAB 250 Xi electron spectrometer with 300 W Al K $\alpha$  radiation; the obtained spectra were corrected with C 1s (284.8 eV). Fourier transform-infrared (FT-IR) spectroscopy was performed on a Nicolet iS50 spectrometer (Thermo Scientific, USA), and specific surface areas and pore structures were measured using a Micromeritics ASAP 3020 nitrogen adsorption apparatus. To investigate the optical absorption properties of the prepared samples, diffuse reflectance spectra (DRS) were recorded on a UV–vis spectrometer (UV 2550, Shimadzu, Japan) equipped with an integrating sphere; here, BaSO<sub>4</sub> was selected as the reference. Photoluminescence (PL) spectra were recorded on a fluorescence spectrophotometer (F-7000, Hitachi, Japan)

at room temperature and an excitation wavelength of 365 nm. Time-resolved fluorescence measurements were performed on an Edinburgh FLS920 instrument at an excitation wavelength of 400 nm. The electronic properties of the samples were examined by electron paramagnetic resonance (EPR) on a Bruker MEX-nano instrument in the dark at room temperature.

### 2.3. Photocatalytic H<sub>2</sub> generation test

The obtained samples were evaluated in terms of their ability to photocatalyze H<sub>2</sub> generation under visible light. A Xe lamp (350 W) was used as the light source, and a filter ( $\lambda > 420 \text{ nm}$ ) was utilized during the photocatalytic reaction. Before the water splitting test, 1 wt% Pt was loaded onto the sample surface to serve as a cocatalyst through a photo-reduction approach. In a typical procedure, the photocatalyst powder was suspended in deionized water by sonication, a certain amount of H<sub>2</sub>PtCl<sub>6</sub> solution was added to this suspension, and the mixture was exposed to light for 0.5 h to yield photocatalysts loaded with Pt nanoparticles. During the water splitting test, 50 mg of the Pt-loaded photocatalysts was added to 80 mL of triethanolamine (15 vol%) solution, and the mixture was sonicated. Then, the reactor was sealed, purged with high purity N<sub>2</sub> for 0.5 h and irradiated. The H<sub>2</sub> yield was detected by a gas chromatograph equipped with a thermal conductivity detector (TCD).

### 2.4. Fabrication of electrodes and photoelectrochemical measurements

Electrodes were prepared by depositing the photocatalyst powders onto a pre-cleaned fluorine-doped tin oxide (FTO) substrate (1.5 cm  $\times$  2 cm). In a typical procedure, 20 mg of the photocatalyst powders was added to 5 mL of ethanol and 10  $\mu\text{L}$  of Nafion (5 wt%) solution, and the mixture was ground into a homogeneous slurry. The slurry was then coated onto the FTO substrate and allowed to dry naturally, finally yielding the electrode. Photoelectrochemical measurements were performed on Shanghai Chenhua CHI-660C electrochemical workstation by adopting a three-electrode system. The prepared electrodes were used as the working electrode, Ag/AgCl was used as the reference electrode and a Pt plate was introduced as counter electrode. 0.5 M Na<sub>2</sub>SO<sub>4</sub> was used as the electrolyte, and a LED light centered at 420 nm was employed as the light source during the test. Electrochemical impedance spectroscopy (EIS) was performed at a frequency range of 0.1 Hz to 100 kHz and a potential of 0.5 V. Linear sweep voltammetry (LSV) was also carried out at a scan rate of 2 mV s<sup>−1</sup> under light irradiation. Mott–Schottky plots were conducted at the AC frequency of 1 and 2 kHz.

### 2.5. Theoretical calculation methods

First-principles calculations were conducted by adopting the VASP code. The Perdew–Burke–Ernzerhof (PBE) exchange–correlation functional was described by generalized gradient approximation (GGA). The energy cutoff was set to 500 eV, and the Monkhorst–Pack k-point mesh included  $3 \times 3 \times 1$  points. Geometry was optimized with a convergence tolerance of  $1.0 \times 10^{-4} \text{ eV/atom}$ , and the work function was calculated by the following equation:  $\Phi = E_V - E_F$ , where  $E_V$  and  $E_F$  are electrostatic potentials at the vacuum and Fermi levels, respectively.

## 3. Results and discussion

### 3.1. Morphology and structure

Interfacial properties play a key role in the charge carrier diffusion process of various materials [49]. A calcination approach was employed to prepare GD/g-C<sub>3</sub>N<sub>4</sub> hybrids with intimate interface, as shown in Fig. 1. Due to the positive charge of C atoms in the diacetylenic groups of GD [51] and negative charge of N atoms in the residual amino groups

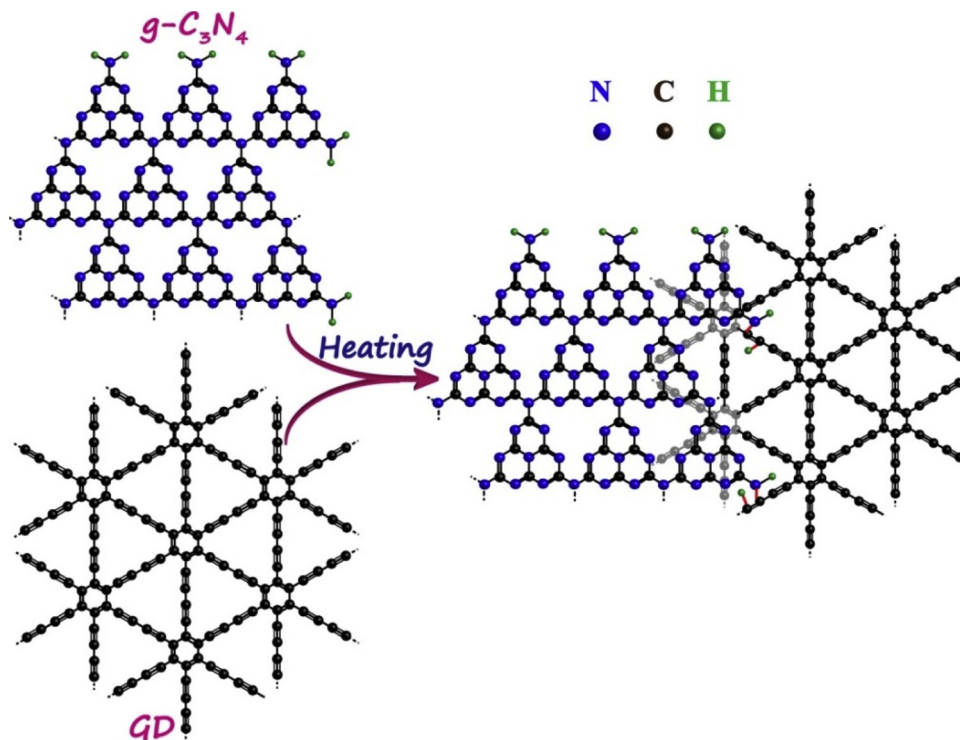


Fig. 1. Schematic illustration of the GD/g-C<sub>3</sub>N<sub>4</sub> hybrid preparation process.

of g-C<sub>3</sub>N<sub>4</sub> [52], a new C–N bond could be expected to form at the GD/g-C<sub>3</sub>N<sub>4</sub> interface after heat treatment, causing strong interactions between GD and g-C<sub>3</sub>N<sub>4</sub>. This strong interaction may facilitate charge carrier migration between g-C<sub>3</sub>N<sub>4</sub> and GD and enhance the photocatalytic performance of the products.

The morphology and microstructure of the prepared photocatalysts were examined by TEM characterization. Fig. 2a and b reveal that GD has large sheet-like micrometer-scale structures without curling, indicating a tough surface. Compared with GD, g-C<sub>3</sub>N<sub>4</sub> shows a distinctly different morphology, featuring silk-like structures with curled edges indicative of a flexible feature (Fig. 2c). An abundance of pores measuring several tens of nanometers are observed in g-C<sub>3</sub>N<sub>4</sub> plane (Fig. 2d). These pores could originate from gas emissions during thermal polymerization of urea [53,54]. This unique microstructure of g-C<sub>3</sub>N<sub>4</sub> contributes to its large specific surface area and benefits reactant diffusion. Figs. 2e and f show TEM images of 0.5%GD/g-C<sub>3</sub>N<sub>4</sub>. The hybrid has a loose and aggregated laminar structure. Owing to the similar atomic number of C and N and the amorphous property of GD and g-C<sub>3</sub>N<sub>4</sub>, differentiating GD from g-C<sub>3</sub>N<sub>4</sub> from the contrast aspect and interplanar spacings observed in the TEM images is difficult. Fortunately, GD and g-C<sub>3</sub>N<sub>4</sub> can be recognized through their different microstructure. As shown in Fig. 2f, portions with a porous structure indicate g-C<sub>3</sub>N<sub>4</sub>, whilst those without can be assigned to GD. This finding suggests the formation of a heterojunction between GD and g-C<sub>3</sub>N<sub>4</sub>.

XRD was employed to investigate the crystal structure of the synthesized samples, as shown in Fig. 3. GD presents a broad and weak diffraction peak centered at about 23°, corresponding to the characteristic (0 0 2) plane of amorphous carbon materials [55,56]. g-C<sub>3</sub>N<sub>4</sub> displays two diffraction peaks at 27.4° and 13.1°, which can be assigned to the (0 0 2) plane originating from interlayer structural packing units and the (1 0 0) plane deduced from interplanar stacking of the conjugated aromatic segments, respectively [40]. The XRD patterns of the GD/g-C<sub>3</sub>N<sub>4</sub> hybrids contain all of the GD and g-C<sub>3</sub>N<sub>4</sub> diffraction peaks, thereby indicating that the crystal structures of GD and g-C<sub>3</sub>N<sub>4</sub> are maintained during the coupling process.

FT-IR spectroscopy was conducted to examine the functional groups of the prepared samples, as shown in Fig. 4. Pure GD displays bands located at 1365 and 1574 cm<sup>−1</sup>, which can be attributed to the stretching vibrations of C–C/C–O bonds and the skeletal vibrations of the benzene ring, respectively. No characteristic band of alkyne groups is observed in GD, which indicates its perfectly symmetrical molecular structure [48]. Pure g-C<sub>3</sub>N<sub>4</sub> shows a series bands in the range of 1200–1700 cm<sup>−1</sup>, which could be assigned to the stretching vibrations of C–N heterocycles [40]. The band located at 805 cm<sup>−1</sup>, which is indicative of the characteristic breathing mode of s-triazine units, can also be observed. Broad bands in the range of 3000–3400 cm<sup>−1</sup> can be assigned to the stretching vibrations of amino groups [15]. The FT-IR spectra of the GD/g-C<sub>3</sub>N<sub>4</sub> hybrids show no distinct change compared with that of g-C<sub>3</sub>N<sub>4</sub>, thus indicating that the structure of g-C<sub>3</sub>N<sub>4</sub> is maintained after coupling, similar to the previous XRD results. Due to the band overlap between the C–N heterocycle and benzene ring and the low content of GD, no distinct bands belonging to GD can be observed in the GD/g-C<sub>3</sub>N<sub>4</sub> hybrids. However, compared with those of pure g-C<sub>3</sub>N<sub>4</sub> and GD, a band shift appears to occur in the GD/g-C<sub>3</sub>N<sub>4</sub> hybrids (Fig. 4b). The band belonging to the C–N heterocycle in the GD/g-C<sub>3</sub>N<sub>4</sub> hybrids shifts towards a higher wavenumber, demonstrating the strong interaction between GD and g-C<sub>3</sub>N<sub>4</sub>, which may originate from  $\pi$ – $\pi$  conjugation or the chemical bond formed between GD and g-C<sub>3</sub>N<sub>4</sub> [48,49,57]. Moreover, peaks belonging to amino groups of the GD/g-C<sub>3</sub>N<sub>4</sub> hybrids exhibit much weaker intensity than those of g-C<sub>3</sub>N<sub>4</sub>, thus suggesting fewer amino groups in the former. This result can be ascribed to the reaction of amino groups of g-C<sub>3</sub>N<sub>4</sub> with the diacetylenic groups of GD.

XPS characterization can provide solid evidence confirming the formation of a new bond between GD and g-C<sub>3</sub>N<sub>4</sub>. Fig. 5a reveals that GD, g-C<sub>3</sub>N<sub>4</sub> and 0.5%GD/g-C<sub>3</sub>N<sub>4</sub> consist of C, N and O. The N and O elements in GD originate from its precursor and adsorbed air, respectively [44], whilst the O elements in g-C<sub>3</sub>N<sub>4</sub> and 0.5%GD/g-C<sub>3</sub>N<sub>4</sub> hybrid stem from incompletely reacted oxygen-containing groups formed during thermal condensation process [58]. Fig. 5b displays the high resolution C 1s XPS spectra of the samples. The C 1s XPS spectrum of



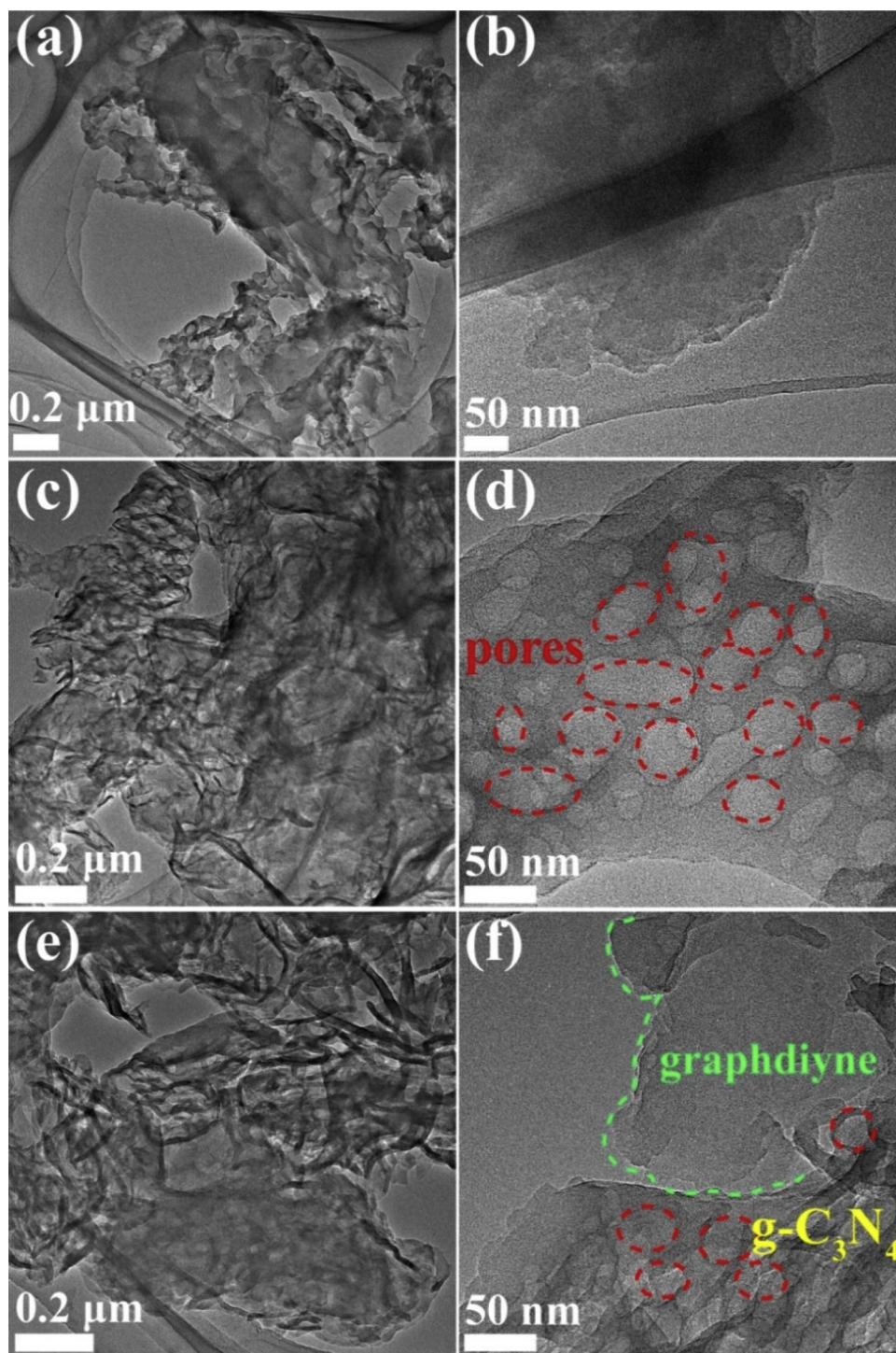


Fig. 2. TEM images of (a,b) GD, (c,d) g-C<sub>3</sub>N<sub>4</sub> and (e,f) 0.5%GD/g-C<sub>3</sub>N<sub>4</sub>.

GD can be deconvoluted into four peaks with binding energies of 284.5, 285.0, 286.7 and 288.2 eV, which are assigned to C=C with  $sp^2$  hybrid orbitals, C≡C with  $sp$  hybrid orbitals, C–O and C=O, respectively. The area ratio between  $sp^2$  and  $sp$  carbons is approximately 0.5, consistent with previous reports [44,48]; this result reveals that GD comprises benzene rings linked to diene groups. The C 1s XPS spectrum of g-C<sub>3</sub>N<sub>4</sub> can be fitted to three peaks with binding energies of 284.8, 286.4 and 288.3 eV, which are respectively attributed to residual C, C–O and  $sp^2$  C in the C–N heterocycle. A new peak at 286.8 eV, indicating the formation of a new C–N bond between GD and g-C<sub>3</sub>N<sub>4</sub>, is observed in the XPS spectrum of the 0.5%GD/g-C<sub>3</sub>N<sub>4</sub> hybrid. This result can be

confirmed by analyzing the high-resolution N 1s XPS spectra of the samples. After deconvoluting the g-C<sub>3</sub>N<sub>4</sub> N 1s XPS spectrum, four peaks with binding energies of 398.8, 400.1, 401.3 and 404.8 eV that can respectively be assigned to  $sp^2$  N in the C–N heterocycle, tertiary N, amino groups and charge effects are obtained [12,59,60]. Compared with that of pure g-C<sub>3</sub>N<sub>4</sub>, a new peak at 400.5 eV can be observed in the N 1s XPS spectrum of 0.5%GD/g-C<sub>3</sub>N<sub>4</sub> (Fig. 5c), and this peak can be assigned to the N–C bond. Considering the  $sp^2$  C in GD is positively charged deduced from the charge distribution [51], the negative  $sp^2$  N in g-C<sub>3</sub>N<sub>4</sub> [52] can come close to the  $sp$  C in GD and react with it during the calcination process. The chemical bond formed between GD and g-

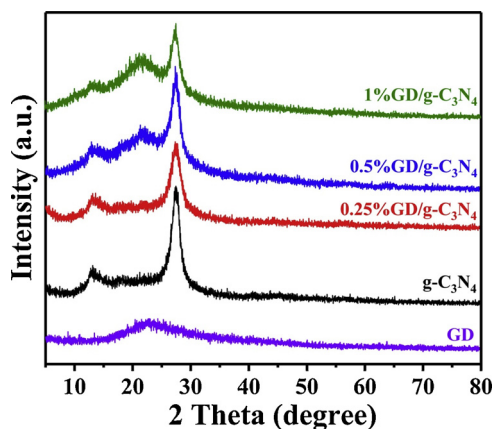


Fig. 3. XRD patterns of the prepared samples.

$\text{C}_3\text{N}_4$  can serve as a charge transfer channel to improve the performance of the photocatalyst. The O 1s spectrum of GD shown in Fig. 5d shows a broad peak, corresponding to adsorbed  $\text{O}_2$  [44].  $\text{g-C}_3\text{N}_4$  and 0.5%GD/ $\text{g-C}_3\text{N}_4$  display peaks at approximately 532.6 eV, which can be assigned to oxygen-containing groups.

The pore structure and specific surface area of the generated photocatalysts were investigated by  $\text{N}_2$  adsorption-desorption isotherms. Both  $\text{g-C}_3\text{N}_4$  and 0.5%GD/ $\text{g-C}_3\text{N}_4$  feature type-IV isotherms with H3 hysteresis loops (Fig. 6a), thus suggesting the presence of mesopores. The textural properties of the as-prepared samples are summarized in Table 1.  $\text{g-C}_3\text{N}_4$  and the GD/ $\text{g-C}_3\text{N}_4$  composites possess similar specific surface areas and pore structures, thereby revealing that introduction of GD to  $\text{g-C}_3\text{N}_4$  to form GD/ $\text{g-C}_3\text{N}_4$  composites does not alter the original microstructure of the photocatalyst.

### 3.2. Photocatalytic performance

Before the photocatalytic water splitting reaction, 1 wt% Pt was deposited onto the photocatalyst surface via a photoreduction approach to serve as a cocatalyst for collecting photogenerated electrons and reducing the water reduction overpotential. During the test, triethanolamine was used as the sacrificial reagent to consume photogenerated holes. When exposed to visible light, the  $\text{H}_2$  generation rate of  $\text{g-C}_3\text{N}_4$  is only  $5.9 \mu\text{mol h}^{-1}$  (Fig. 7a). After combining with GD, the  $\text{H}_2$  evolution rate of the obtained hybrids increases and reaches  $39.6 \mu\text{mol h}^{-1}$ , exceeding that of  $\text{g-C}_3\text{N}_4$  by 6.7-fold, at a GD loading of 0.5 wt%. However, further increases in GD ratio decrease the  $\text{H}_2$  generation rate, likely because excess GD disrupts the subtle balance between charge carrier separation and light utilization efficiency. GD shows strong light absorption and can compete with  $\text{g-C}_3\text{N}_4$  for light,

thus weakening the light utilization efficiency of the latter. Excess GD would overwhelm the benefits of improved charge separation, causing poor photocatalytic activity. Stability is an important parameter in the evaluation of a photocatalyst. Fig. 7b displays the recycle ability of 0.5%GD/ $\text{g-C}_3\text{N}_4$  for the  $\text{H}_2$  evolution reaction. 0.5%GD/ $\text{g-C}_3\text{N}_4$  displays no significantly loss in  $\text{H}_2$  yield after running for four cycles (3 h each cycle), thereby indicating its excellent stability. In comparison with previously reported carbonaceous/ $\text{g-C}_3\text{N}_4$  composites (Table 2), the synthesized GD/ $\text{g-C}_3\text{N}_4$  hybrids display superior or comparable photocatalytic  $\text{H}_2$  evolution performance. These results reveal that GD exerts positive effects on  $\text{g-C}_3\text{N}_4$ .

### 3.3. Mechanism evaluation

The photoelectrochemical performance of the prepared samples was systematically investigated and compared. Mott-Schottky plots were employed to evaluate the band structure of the samples and verify whether they satisfy the potential requirement for proton reduction. Fig. 8a demonstrates that the flat band potentials of  $\text{g-C}_3\text{N}_4$  and 0.5%GD/ $\text{g-C}_3\text{N}_4$  are  $-1.63$  and  $-1.29$  V (vs. Ag/AgCl at pH 7), respectively. These values can respectively be converted to  $-1.02$  and  $-0.68$  V versus the normal hydrogen electrode (NHE), respectively. Apparently, both  $\text{g-C}_3\text{N}_4$  and 0.5%GD/ $\text{g-C}_3\text{N}_4$  are n-type semiconductors because their Mott-Schottky plots show positive slopes. As the CB potential of n-type semiconductors is more negative by approximately  $-0.1$  to  $-0.3$  V than their flat band potential [66], the resultant samples meet the thermodynamic requirements and possess sufficient driving force for water reduction. 0.5%GD/ $\text{g-C}_3\text{N}_4$  exhibits a smaller slope relative to that of  $\text{g-C}_3\text{N}_4$ , thus indicating intensified electron density in the former [67]. Higher electron densities benefit electric conductivity and charge carrier mobility, and favor improvements in photocatalytic performance. The LSV polarization curves of the samples were recorded under light irradiation, as shown in Fig. 8b. Whilst 1%Pt/0.5%GD/ $\text{g-C}_3\text{N}_4$  requires an overpotential of  $-0.75$  V for  $0.1 \text{ mA cm}^{-2}$ , 1%Pt/ $\text{g-C}_3\text{N}_4$  requires a larger overpotential of  $-0.81$  V to drive  $0.1 \text{ mA cm}^{-2}$ . 1%Pt/0.5%GD/ $\text{g-C}_3\text{N}_4$  exhibits a remarkably enhanced photocurrent intensity ( $0.9 \mu\text{A cm}^{-2}$ ), which is about 4.5-fold that of  $\text{g-C}_3\text{N}_4$  ( $0.2 \mu\text{A cm}^{-2}$ ) (Fig. 8c), indicating its high electron-hole separation efficiency. EIS was further performed to understand the transfer and separation efficiency of photogenerated charge carriers in the prepared samples, and the results are illustrated in Fig. 8d. In general, a small arc radius indicates low charge-transfer resistance. 1%Pt/0.5%GD/ $\text{g-C}_3\text{N}_4$  shows a lower charge transfer resistance than 1%Pt/ $\text{g-C}_3\text{N}_4$ .

The light harvesting properties of the prepared samples play a key role in producing charge carriers. Thus, DRB characterization was conducted. Fig. 9a reveals that the intrinsic absorption edge of  $\text{g-C}_3\text{N}_4$  is about 440 nm, corresponding to a band gap of 2.8 eV.  $\text{g-C}_3\text{N}_4$  and the

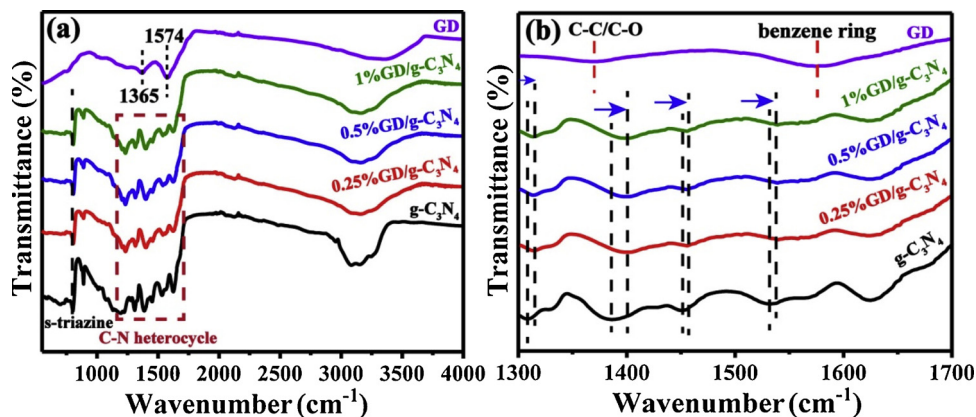


Fig. 4. (a) FT-IR spectra of different samples. (b) Enlarged FT-IR spectra from (a).



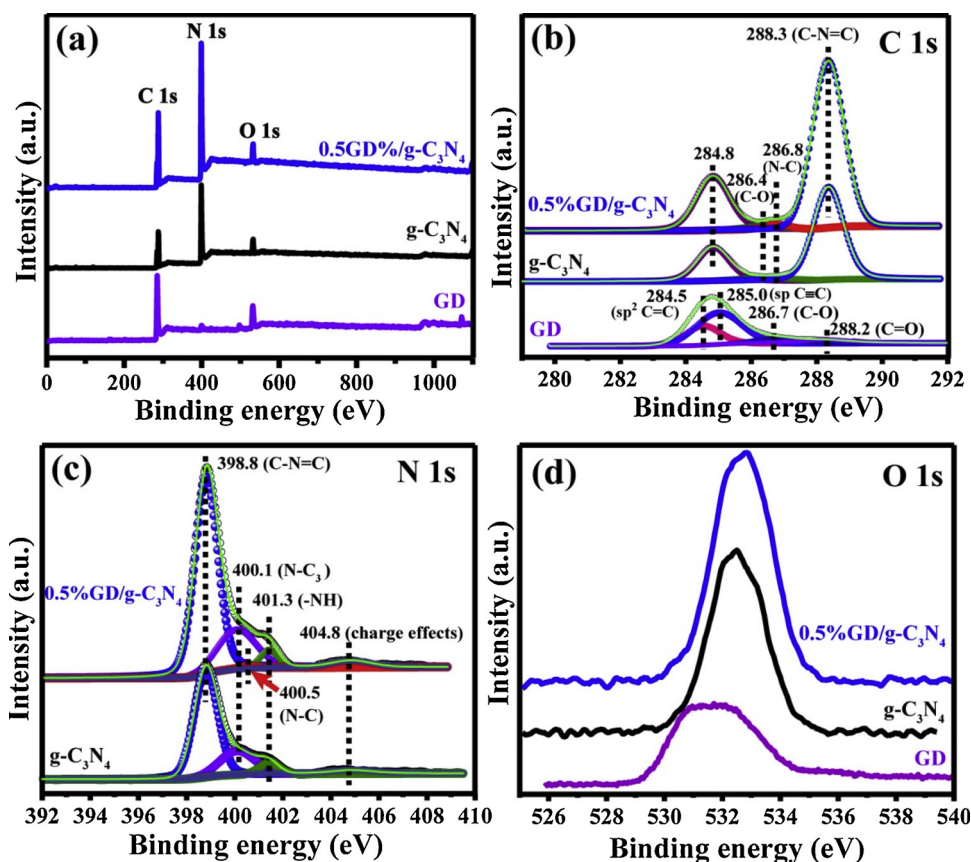


Fig. 5. XPS spectra of GD, g-C<sub>3</sub>N<sub>4</sub> and 0.5%GD/g-C<sub>3</sub>N<sub>4</sub>: (a) survey spectra and high resolution spectra of (b) C 1s, (c) N 1s and (d) O 1s.

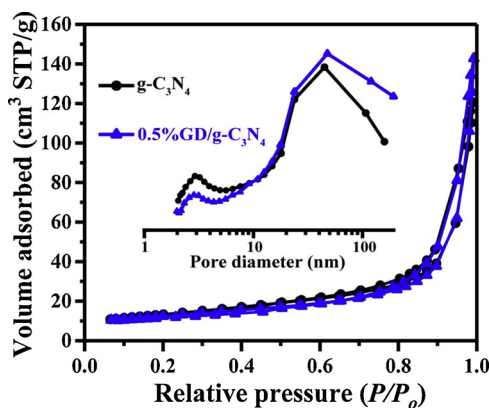


Fig. 6. N<sub>2</sub> adsorption–desorption isotherms of g-C<sub>3</sub>N<sub>4</sub> and 0.5%GD/g-C<sub>3</sub>N<sub>4</sub>. The pore size distribution is also indicated.

Table 1

Textural properties of the prepared samples.

Samples	S <sub>BET</sub> (m <sup>2</sup> /g)	Average pore size (nm)	Pore volume (cm <sup>3</sup> /g)
g-C <sub>3</sub> N <sub>4</sub>	41	15.8	0.19
0.25%GD/g-C <sub>3</sub> N <sub>4</sub>	40	21.5	0.21
0.5%GD/g-C <sub>3</sub> N <sub>4</sub>	43	20.4	0.22
1%GD/g-C <sub>3</sub> N <sub>4</sub>	44	20.8	0.23

GD/g-C<sub>3</sub>N<sub>4</sub> hybrids display the same absorption edge, indicating that the chemical bond formed between GD and g-C<sub>3</sub>N<sub>4</sub> does not affect the band structure. In contrast to g-C<sub>3</sub>N<sub>4</sub>, the GD/g-C<sub>3</sub>N<sub>4</sub> hybrids exhibit intensified light harvesting capacity over the entire detection range, corresponding to the color change from light yellow (g-C<sub>3</sub>N<sub>4</sub>) to light

grey (1.0%GD/g-C<sub>3</sub>N<sub>4</sub>). The PL results support the notion that both hybrids and pure g-C<sub>3</sub>N<sub>4</sub> display the same absorption edge. As presented in Fig. 9b, both g-C<sub>3</sub>N<sub>4</sub> and 0.5%GD/g-C<sub>3</sub>N<sub>4</sub> show a broad emission peak centered at 440 nm, which is originates from band–band recombination. The emission peak intensity of 0.5%GD/g-C<sub>3</sub>N<sub>4</sub> significantly decreases relative to that of g-C<sub>3</sub>N<sub>4</sub>, indicating efficiently suppressed electron–hole recombination.

The time-resolved fluorescence decay spectra of g-C<sub>3</sub>N<sub>4</sub> and 0.5%GD/g-C<sub>3</sub>N<sub>4</sub> were examined to extensively analyze the photo-physical processes of their photogenerated charge carriers. The emission decay profiles of g-C<sub>3</sub>N<sub>4</sub> and 0.5%GD/g-C<sub>3</sub>N<sub>4</sub> can be fitted by a two-exponential decay model, and their lifetimes are summarized in Fig. 9c. The fast decay components of the profiles are derived from the non-radiative process involving photoinduced electron capture, and the slow decay components are assigned to the interband recombination of free-excitons [67,68]. 0.5%GD/g-C<sub>3</sub>N<sub>4</sub> (average decay lifetime, 5.9 ns) displays slow decay kinetics relative to that of g-C<sub>3</sub>N<sub>4</sub> (average decay lifetime, 5.5 ns). Compared with those of g-C<sub>3</sub>N<sub>4</sub>, both short and long lifetime of 0.5%GD/g-C<sub>3</sub>N<sub>4</sub> is prolonged, indicating suppressed recombination of photoinduced charge carriers in the latter. The prolonged lifetime of photogenerated charge carriers can improve the participation of these carriers in the photocatalytic reaction, thus benefiting the photocatalytic performance of the samples.

Fig. 9d shows the EPR spectra of the as-prepared samples at room temperature. Both g-C<sub>3</sub>N<sub>4</sub> and 0.5%GD/g-C<sub>3</sub>N<sub>4</sub> display a single Lorentzian line with a g value of 2.003, which is attributed to the existence of lone electron pairs on the odd sp<sup>2</sup> carbon atoms of the heptazine rings [69]. GD exhibits a similar lineshape with a different g value of 2.0028, which originates from fringe non-bonding  $\pi$  electrons [70]. Interestingly, 0.5%GD/g-C<sub>3</sub>N<sub>4</sub> exhibits an intensified EPR signal relative to that of g-C<sub>3</sub>N<sub>4</sub>, thus revealing remarkable delocalization and a high concentration of unpaired electrons in the sample. These features

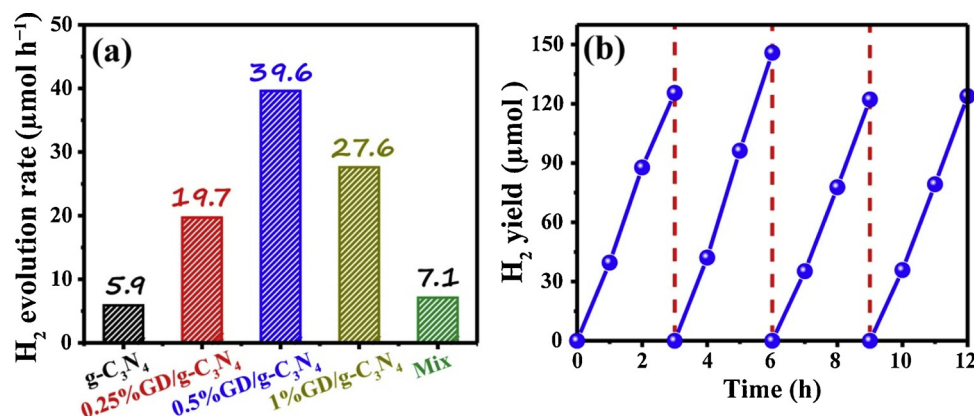


Fig. 7. (a) Photocatalytic  $\text{H}_2$  evolution rate of the prepared samples under visible light ( $\lambda > 420 \text{ nm}$ ). (b) Stability of 0.5%GD/g- $\text{C}_3\text{N}_4$  during photocatalytic  $\text{H}_2$  evolution.

Table 2

Comparison of the photocatalytic  $\text{H}_2$  generation achieved by the g- $\text{C}_3\text{N}_4$ -based photocatalysts.

Photocatalyst	Co-catalyst	Light source	Measurement conditions	Rate of $\text{H}_2$ evolution ( $\mu\text{mol h}^{-1}$ )	Ref.
GD/g- $\text{C}_3\text{N}_4$	1 wt% Pt	350 W Xe lamp ( $\lambda > 420 \text{ nm}$ )	0.05 g photocatalyst, 15 vol% triethanolamine solution	39.6	This work
MWNTs/ g- $\text{C}_3\text{N}_4$	1 wt% Pt	300W Xe lamp ( $\lambda > 400 \text{ nm}$ )	0.1 g photocatalyst, 25 vol% methanol solution	7.58	[61]
CNT/g- $\text{C}_3\text{N}_4$	1.2 wt% Pt	300W Xe lamp ( $\lambda > 420 \text{ nm}$ )	0.1 g photocatalyst, 10 vol% triethanolamine solution	39.4	[62]
g-PAN/g- $\text{C}_3\text{N}_4$	1.5 wt% Pt	300W Xe lamp ( $\lambda > 400 \text{ nm}$ )	0.1 g photocatalyst, 10 vol% triethanolamine solution	37	[63]
Carbon black/g- $\text{C}_3\text{N}_4$	3 wt% Pt	Visible-light	0.1 g photocatalyst, 25 vol% methanol solution	68.9	[64]
Graphene/ g- $\text{C}_3\text{N}_4$	1.5 wt% Pt	350W Xe lamp ( $\lambda > 400 \text{ nm}$ )	0.08 g photocatalyst, 25 vol% methanol solution	36.1	[65]

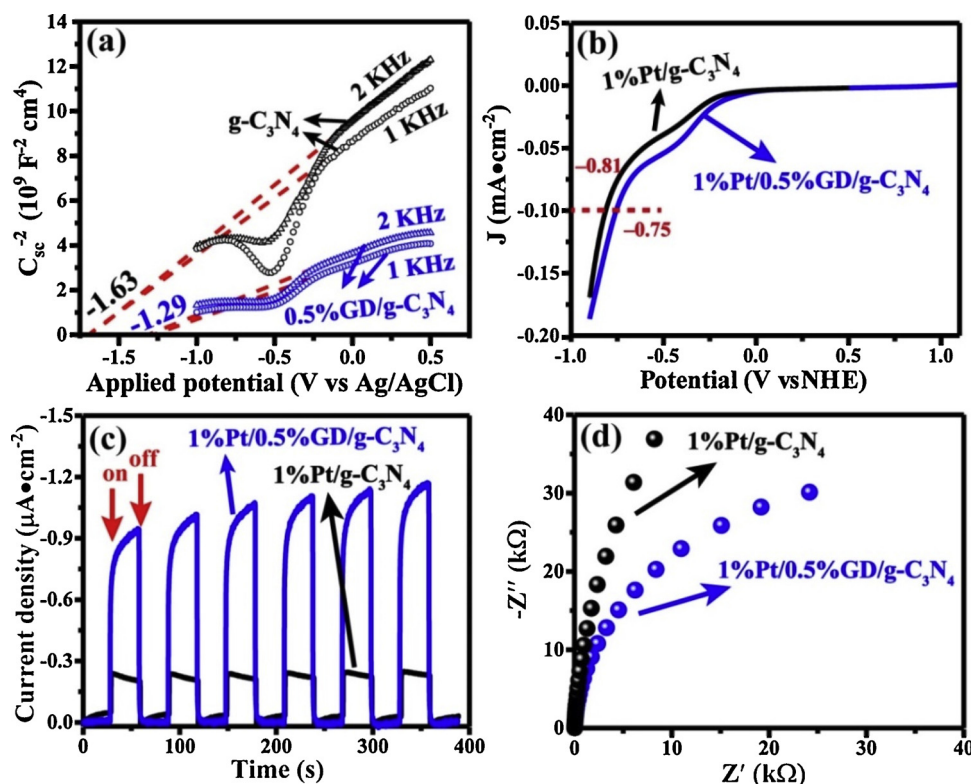


Fig. 8. (a) Mott-Schottky plots, (b) LSV curves, (c) photocurrent curves and (d) EIS plots.

endow 0.5%GD/g- $\text{C}_3\text{N}_4$  with high electron mobility and suppress the recombination of photogenerated electron-hole pairs, thus benefiting the photocatalytic process [71].

The photocatalytic mechanism of GD/g- $\text{C}_3\text{N}_4$  can be speculated as follows. Considering that g- $\text{C}_3\text{N}_4$  possesses a smaller work function (4.3 eV) relative to that of GD (5.14 eV) (Fig. 10), electrons can transfer

from g- $\text{C}_3\text{N}_4$  to GD when they come into contact, thus forming a Schottky barrier [72]. Pt nanoparticles deposit onto the GD surface during the photo-deposition process due to its electron-rich feature. As shown in Fig. 11, when the Pt/GD/g- $\text{C}_3\text{N}_4$  composite is exposed to visible light, the photoinduced electrons accumulate on the CB of g- $\text{C}_3\text{N}_4$  and then transfer to the Pt nanoparticles involved in proton

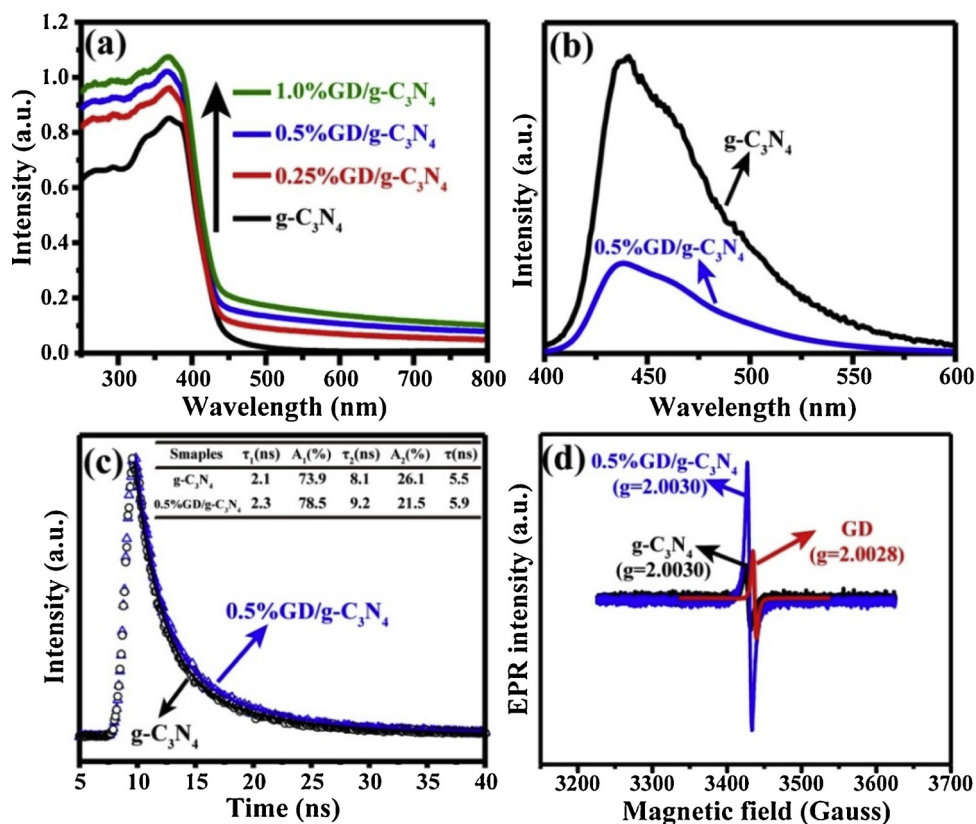


Fig. 9. (a) DRS spectra of g-C<sub>3</sub>N<sub>4</sub> and GD/g-C<sub>3</sub>N<sub>4</sub> hybrids with various GD contents. (b) Steady-state PL spectra, (c) time-resolved transient PL decay, and (d) EPR spectra of g-C<sub>3</sub>N<sub>4</sub>, GD and 0.5%GD/g-C<sub>3</sub>N<sub>4</sub>. The inset in (c) shows the fitted lifetime from the fluorescence decay.

reduction with the help of GD through two routes, namely, the  $\pi$ - $\pi$  configuration (route 1) and the newly formed C-N bond (route 2). Meanwhile, photoexcited holes stay in the VB of g-C<sub>3</sub>N<sub>4</sub> and participate in the TEOA oxidation reaction, thus achieving spatial separation of the photoexcited generated electron-hole pairs.

#### 4. Conclusions

In the present work, GD was employed to modify g-C<sub>3</sub>N<sub>4</sub> and improve its photocatalytic water splitting activity under visible light. After coupling g-C<sub>3</sub>N<sub>4</sub> with GD by calcination treatment, a new C-N bond is formed between GD and g-C<sub>3</sub>N<sub>4</sub>, and this bond serves as the link

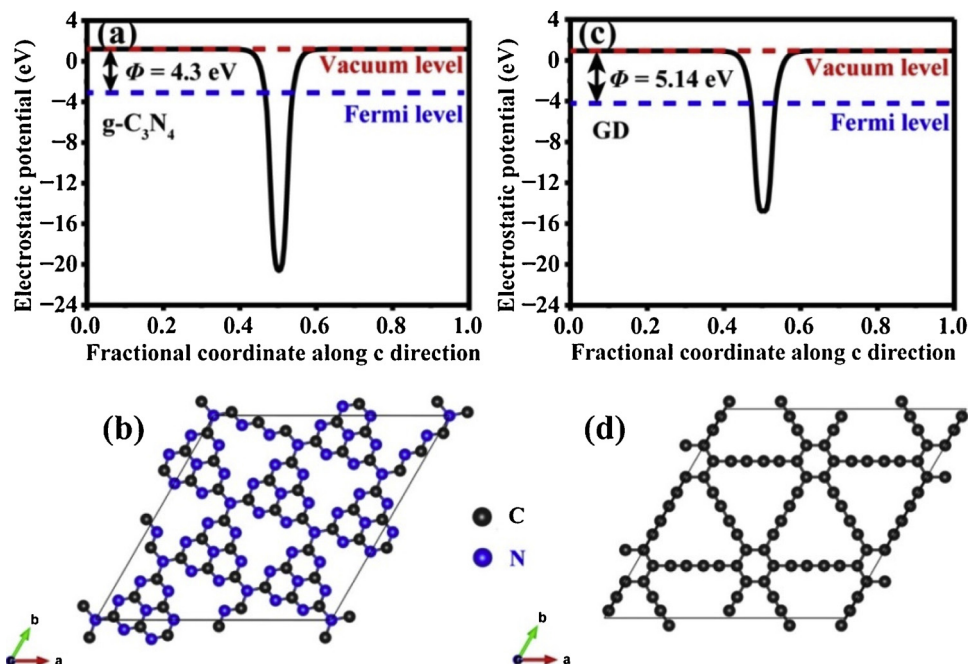


Fig. 10. (a) Calculated electrostatic potentials and (b) top-view of the geometric structure of g-C<sub>3</sub>N<sub>4</sub>. (c) Calculated electrostatic potentials and (d) top-view of the geometric structure of GD.



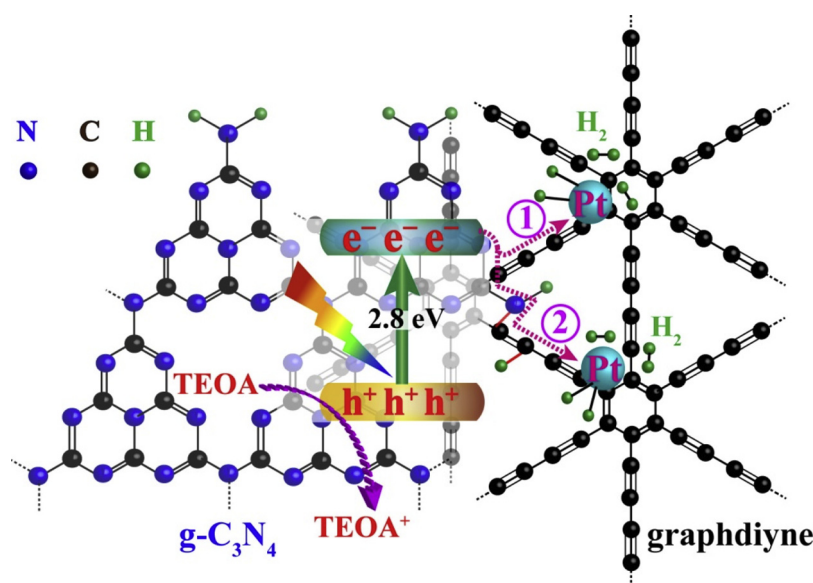


Fig. 11. Photocatalytic mechanism of GD/g-C<sub>3</sub>N<sub>4</sub> after loading with Pt nanoparticles.

through which photogenerated charge carrier separation and migration are facilitated. The photocatalytic activity of the hybrid is dependent on the GD content, and a maximum H<sub>2</sub> generation rate of 39.6  $\mu\text{mol h}^{-1}$ , exceeding that of g-C<sub>3</sub>N<sub>4</sub> by 6.7-fold, is achieved when the GD content is 0.5 wt%. The GD/g-C<sub>3</sub>N<sub>4</sub> hybrids possess superior photocatalytic performance as a result of their prolonged photogenerated charge carrier lifetime, intensified electron density, decreased reaction overpotential and improved electron mobility. This work provides a new paradigm in solar to chemical energy conversion.

### Acknowledgements

This work was supported by The National Key Research and Development Program of China (2018YFB1502001), NSFC (U1705251, 21573170, 21433007 and 21871217), the Innovative Research Funds of SKLWUT (2017-ZD-4) and Dean's Research Fund 2016-17 (ref: 04725), EdUHK.

### References

- H. Zou, B. He, P. Kuang, J. Yu, K. Fan, Ni<sub>3</sub>S<sub>2</sub> nanowalls/nitrogen-doped graphene foam is an efficient trifunctional catalyst for unassisted artificial photosynthesis, *Adv. Funct. Mater.* 28 (2018) 1706917.
- Y. Xu, M. Kraft, R. Xu, Metal-free carbonaceous electrocatalysts and photocatalysts for water splitting, *Chem. Soc. Rev.* 45 (2016) 3039–3052.
- J. Fu, B. Zhu, W. You, M. Jaroniec, J. Yu, A flexible bio-inspired H<sub>2</sub>-production photocatalyst, *Appl. Catal. B* 220 (2018) 148–160.
- X. Li, J. Yu, M. Jaroniec, X. Chen, Cocatalysts for selective photoreduction of CO<sub>2</sub> into solar fuels, *Chem. Rev.* 119 (2019) 3962–4179.
- R. Shen, C. Jiang, Q. Xiang, J. Xie, X. Li, Surface and interface engineering of hierarchical photocatalysts, *Appl. Surf. Sci.* 471 (2019) 43–87.
- L. Li, Z. Cai, Q. Wu, W.Y. Lo, N. Zhang, L.X. Chen, L. Yu, Rational design of porous conjugated polymers and roles of residual palladium for photocatalytic hydrogen production, *J. Am. Chem. Soc.* 138 (2016) 7681–7686.
- D. Feng, Y. Cheng, J. He, L. Zheng, D. Shao, W. Wang, W. Wang, F. Lu, H. Dong, H. Liu, R. Zheng, H. Liu, Enhanced photocatalytic activities of g-C<sub>3</sub>N<sub>4</sub> with large specific surface area via a facile one-step synthesis process, *Carbon* 125 (2017) 454–463.
- B. Zhu, L. Zhang, B. Cheng, J. Yu, First-principle calculation study of tri-s-triazine-based g-C<sub>3</sub>N<sub>4</sub>: a review, *Appl. Catal. B* 224 (2018) 983–999.
- J. Fu, C. Bie, B. Cheng, C. Jiang, J. Yu, Hollow CoS<sub>x</sub> polyhedrons act as high-efficiency cocatalyst for enhancing the photocatalytic hydrogen generation of g-C<sub>3</sub>N<sub>4</sub>, *ACS Sustain. Chem. Eng.* 6 (2018) 2767–2779.
- X. Wang, K. Maeda, A. Thomas, K. Takanabe, G. Xin, J.M. Carlsson, K. Domen, M. Antonietti, A metal-free polymeric photocatalyst for hydrogen production from water under visible light, *Nat. Mater.* 8 (2009) 76–80.
- J. Wen, J. Xie, X. Chen, X. Li, A review on g-C<sub>3</sub>N<sub>4</sub>-based photocatalysts, *Appl. Surf. Sci.* 391 (2017) 72–123.
- F. Wu, X. Li, W. Liu, S. Zhang, Highly enhanced photocatalytic degradation of methylene blue over the indirect all-solid-state Z-scheme g-C<sub>3</sub>N<sub>4</sub>-RGO-TiO<sub>2</sub> nanoheterojunctions, *Appl. Surf. Sci.* 405 (2017) 60–70.
- J. Zhang, F. Huang, Enhanced visible light photocatalytic H<sub>2</sub> production activity of g-C<sub>3</sub>N<sub>4</sub> via carbon fiber, *Appl. Surf. Sci.* 358 (2015) 287–295.
- Z. Zhang, Y. Zhang, L. Lu, Y. Si, S. Zhang, Y. Chen, K. Dai, P. Duan, L. Duan, J. Liu, Graphitic carbon nitride nanosheet for photocatalytic hydrogen production: the impact of morphology and element composition, *Appl. Surf. Sci.* 391 (2017) 369–375.
- B. Wang, J. Zhang, F. Huang, Enhanced visible light photocatalytic H<sub>2</sub> evolution of metal-free g-C<sub>3</sub>N<sub>4</sub>/SiC heterostructured photocatalysts, *Appl. Surf. Sci.* 391 (2017) 449–456.
- W. Yu, J. Chen, T. Shang, L. Chen, L. Gu, T. Peng, Direct Z-scheme g-C<sub>3</sub>N<sub>4</sub>/WO<sub>3</sub> photocatalyst with atomically defined junction for H<sub>2</sub> production, *Appl. Catal. B* 219 (2017) 693–704.
- X. Lu, J. Xie, S. Liu, A. Adamski, X. Chen, X. Li, Low-cost Ni<sub>3</sub>B/Ni(OH)<sub>2</sub> as an ecofriendly hybrid cocatalyst for remarkably boosting photocatalytic H<sub>2</sub> production over g-C<sub>3</sub>N<sub>4</sub> nanosheets, *ACS Sustain. Chem. Eng.* 6 (2018) 13140–13150.
- X. Wang, X. Chen, A. Thomas, X. Fu, M. Antonietti, Metal-containing carbon nitride compounds: A new functional organic–metal hybrid material, *Adv. Mater.* 21 (2009) 1609–1612.
- W. Jiang, W. Luo, J. Wang, M. Zhang, Y. Zhu, Enhancement of catalytic activity and oxidative ability for graphitic carbon nitride, *J. Photochem. Photobiol. C Photochem. Rev.* 28 (2016) 87–115.
- J. Fu, Q. Xu, J. Low, C. Jiang, J. Yu, Ultrathin 2D/2D WO<sub>3</sub>/g-C<sub>3</sub>N<sub>4</sub> step-scheme H<sub>2</sub>-production photocatalyst, *Appl. Catal. B* 243 (2019) 556–565.
- C. Li, S. Yu, H. Che, X. Zhang, J. Han, Y. Mao, Y. Wang, C. Liu, H. Dong, Fabrication of Z-scheme heterojunction by anchoring mesoporous  $\gamma$ -Fe<sub>2</sub>O<sub>3</sub> nanospheres on g-C<sub>3</sub>N<sub>4</sub> for degrading tetracycline hydrochloride in water, *ACS Sustain. Chem. Eng.* 6 (2018) 16437–16447.
- C. Li, S. Yu, H. Dong, C. Liu, H. Wu, H. Che, G. Chen, Z-scheme mesoporous photocatalyst constructed by modification of Sn<sub>3</sub>O<sub>4</sub> nanoclusters on g-C<sub>3</sub>N<sub>4</sub> nanosheets with improved photocatalytic performance and mechanism insight, *Appl. Catal. B* 238 (2018) 284–293.
- Z. Tong, D. Yang, Z. Li, Y. Nan, F. Ding, Y. Shen, Z. Jiang, Thylakoid-inspired multishell g-C<sub>3</sub>N<sub>4</sub> nanocapsules with enhanced visible-light harvesting and electron transfer properties for high-efficiency photocatalysis, *ACS Nano* 11 (2017) 1103–1112.
- Y. Hong, C. Li, Z. Fang, B. Luo, W. Shi, Rational synthesis of ultrathin graphitic carbon nitride nanosheets for efficient photocatalytic hydrogen evolution, *Carbon* 121 (2017) 463–471.
- J. Zhang, X. Chen, K. Takanabe, K. Maeda, K. Domen, J.D. Epping, X. Fu, M. Antonietti, X. Wang, Synthesis of a carbon nitride structure for visible-light catalysis by copolymerization, *Angew. Chem. Int. Ed.* 49 (2010) 441–444.
- J. Fu, B. Zhu, C. Jiang, B. Cheng, W. You, J. Yu, Hierarchical porous O-doped g-C<sub>3</sub>N<sub>4</sub> with enhanced photocatalytic CO<sub>2</sub> reduction activity, *Small* 13 (2017) 1603938.
- Q. Fan, J. Liu, Y. Yu, S. Zuo, B. Li, A simple fabrication for sulfur doped graphitic carbon nitride porous rods with excellent photocatalytic activity degrading RhB dye, *Appl. Surf. Sci.* 391 (2017) 360–368.
- J. Jiang, S. Cao, C. Hu, C. Chen, A comparison study of alkali metal-doped g-C<sub>3</sub>N<sub>4</sub> for visible-light photocatalytic hydrogen evolution, *Chin. J. Catal.* 38 (2017) 1981–1989.
- C. Li, S. Yu, X. Zhang, Y. Wang, C. Liu, G. Chen, H. Dong, Insight into photocatalytic activity, universality and mechanism of copper/chlorine surface dual-doped graphitic carbon nitride for degrading various organic pollutants in water, *J. Colloid*

- Interf. Sci. 538 (2019) 462–473.
- [30] T. Di, B. Zhu, B. Cheng, J. Yu, J. Xu, A direct Z-scheme g-C<sub>3</sub>N<sub>4</sub>/SnS<sub>2</sub> photocatalyst with superior visible-light CO<sub>2</sub> reduction performance, *J. Catal.* 352 (2017) 532–541.
- [31] M. Wang, M. Shen, L. Zhang, J. Tian, X. Jin, Y. Zhou, J. Shi, 2D-2D MnO<sub>2</sub>/g-C<sub>3</sub>N<sub>4</sub> heterojunction photocatalyst: in-situ synthesis and enhanced CO<sub>2</sub> reduction activity, *Carbon* 120 (2017) 23–31.
- [32] Q. Xu, B. Zhu, C. Jiang, B. Cheng, J. Yu, Constructing 2D/2D Fe<sub>2</sub>O<sub>3</sub>/g-C<sub>3</sub>N<sub>4</sub> direct Z-scheme photocatalysts with enhanced H<sub>2</sub> generation performance, *Sol. RRL* 2 (2018) 1800006.
- [33] J. Fu, J. Yu, C. Jiang, B. Cheng, g-C<sub>3</sub>N<sub>4</sub>-based heterostructured photocatalysts, *Adv. Energy Mater.* 8 (2018) 1701503.
- [34] F. Chen, H. Yang, W. Luo, P. Wang, H. Yu, Selective adsorption of thiocyanate anions on Ag-modified g-C<sub>3</sub>N<sub>4</sub> for enhanced photocatalytic hydrogen evolution, *Chin. J. Catal.* 38 (2017) 1990–1998.
- [35] P. Zhang, T. Wang, H. Zeng, Design of Cu-Cu<sub>2</sub>O/g-C<sub>3</sub>N<sub>4</sub> nanocomponent photocatalysts for hydrogen evolution under visible light irradiation using water-soluble Erythrosin B dye sensitization, *Appl. Surf. Sci.* 391 (2017) 404–414.
- [36] C. Li, S. Yu, H. Dong, Y. Wang, H. Wu, X. Zhang, G. Chen, C. Liu, Mesoporous ferrihydrite nanoreactors modified on graphitic carbon nitride towards improvement of physical, photoelectrochemical properties and photocatalytic performance, *J. Colloid Interf. Sci.* 531 (2018) 331–342.
- [37] C. Li, S. Yu, L. Gu, J. Han, H. Dong, Y. Wang, G. Chen, A new graphitic carbon nitride/horseradish peroxidase hybrid nano-bio artificial catalytic system for unselective degradation of persistent phenolic pollutants, *Adv. Mater. Interfaces* (2018) 1801297.
- [38] Y. Zhou, L. Zhang, W. Huang, Q. Kong, X. Fan, M. Wang, J. Shi, N-doped graphitic carbon-incorporated g-C<sub>3</sub>N<sub>4</sub> for remarkably enhanced photocatalytic H<sub>2</sub> evolution under visible light, *Carbon* 99 (2016) 111–117.
- [39] R. Shen, W. Liu, D. Ren, J. Xie, X. Li, Co<sub>1.4</sub>Ni<sub>0.6</sub>P cocatalysts modified metallic carbon black/g-C<sub>3</sub>N<sub>4</sub> nanosheet Schottky heterojunctions for active and durable photocatalytic H<sub>2</sub> production, *Appl. Surf. Sci.* 466 (2019) 393–400.
- [40] Q. Xu, C. Jiang, B. Cheng, J. Yu, Enhanced visible-light photocatalytic H<sub>2</sub>-generation activity of carbon/g-C<sub>3</sub>N<sub>4</sub> nanocomposites prepared by two-step thermal treatment, *Dalton Trans.* 46 (2017) 10611–10619.
- [41] W. Xing, C. Li, G. Chen, Z. Han, Y. Zhou, Y. Hu, Q. Meng, Incorporating a novel metal-free interlayer into g-C<sub>3</sub>N<sub>4</sub> framework for efficiency enhanced photocatalytic H<sub>2</sub> evolution activity, *Appl. Catal. B* 203 (2017) 65–71.
- [42] Q. Xu, B. Cheng, J. Yu, G. Liu, Making co-condensed amorphous carbon/g-C<sub>3</sub>N<sub>4</sub> composites with improved visible-light photocatalytic H<sub>2</sub>-production performance using Pt as cocatalyst, *Carbon* 118 (2017) 241–249.
- [43] J. Wen, J. Xie, Z. Yang, R. Shen, H. Li, X. Luo, X. Chen, X. Li, Fabricating the robust g-C<sub>3</sub>N<sub>4</sub> nanosheets/carbon/NiS multiple heterojunctions for enhanced photocatalytic H<sub>2</sub> generation: an insight into the trifunctional roles of nanocarbons, *ACS Sustain. Chem. Eng.* 5 (2017) 2224–2236.
- [44] G. Li, Y. Li, H. Liu, Y. Guo, Y. Li, D. Zhu, Architecture of graphdiyne nanoscale films, *Chem. Commun.* 46 (2010) 3256–3258.
- [45] Y. Li, L. Xu, H. Liu, Y. Li, Graphdiyne and graphyne: from theoretical predictions to practical construction, *Chem. Soc. Rev.* 43 (2014) 2572–2586.
- [46] Y. Han, X. Lu, S. Tang, X. Yin, Z. Wei, T. Lu, Metal-free 2D/2D heterojunction of graphitic carbon nitride/graphdiyne for improving the hole mobility of graphitic carbon nitride, *Adv. Energy Mater.* 8 (2018) 1702992.
- [47] M. Long, L. Tang, D. Wang, Y. Li, Z. Shuai, Electronic structure and carrier mobility in graphdiyne sheet and nanoribbons: theoretical predictions, *ACS Nano* 5 (2011) 2593–2600.
- [48] S. Wang, L. Yi, J.E. Halpert, X. Lai, Y. Liu, H. Cao, R. Yu, D. Wang, Y. Li, A novel and highly efficient photocatalyst based on P25-graphdiyne nanocomposite, *Small* 8 (2012) 265–271.
- [49] N. Yang, Y. Liu, H. Wen, Z. Tang, H. Zhao, Y. Li, Dan Wang, Photocatalytic properties of graphdiyne and graphene modified TiO<sub>2</sub>: from theory to experiment, *ACS Nano* 7 (2013) 1504–1512.
- [50] X. Qian, Z. Ning, Y. Li, H. Liu, C. Ouyang, Q. Chen, Y. Li, Construction of graphdiyne nanowires with high-conductivity and mobility, *Dalton Trans.* 41 (2012) 730–733.
- [51] P. Wu, P. Du, H. Zhang, C. Cai, Graphdiyne as a metal-free catalyst for low-temperature CO oxidation, *Phys. Chem. Chem. Phys.* 16 (2014) 5640–5648.
- [52] Y. Gong, M. Li, Y. Wang, Carbon nitride in energy conversion and storage: recent advances and future prospects, *ChemSusChem* 8 (2015) 931–946.
- [53] J. Mao, T. Peng, X. Zhang, K. Li, L. Ye, L. Zan, Effect of graphitic carbon nitride microstructures on the activity and selectivity of photocatalytic CO<sub>2</sub> reduction under visible light, *Catal. Sci. Technol.* 3 (2013) 1253–1260.
- [54] Y. Hou, Z. Wen, S. Cui, X. Guo, J. Chen, Constructing 2D porous graphitic C<sub>3</sub>N<sub>4</sub> nanosheets/nitrogen-doped graphene/layered MoS<sub>2</sub> ternary nanojunction with enhanced photoelectrochemical activity, *Adv. Mater.* 25 (2013) 6291–6297.
- [55] G. Panomsuwan, N. Saito, T. Ishizaki, Nitrogen-doped carbon nanoparticle-carbon nanofiber composite as an efficient metal-free cathode catalyst for oxygen reduction reaction, *ACS Appl. Mater. Interfaces* 8 (2016) 6962–6971.
- [56] M. Okamura, A. Takagaki, M. Toda, J.N. Kondo, K. Domen, T. Tatsumi, M. Hara, S. Hayashi, Acid-catalyzed reactions on flexible polycyclic aromatic carbon in amorphous carbon, *Chem. Mater.* 18 (2006) 3039–3045.
- [57] C. Kuang, G. Tang, T. Jiu, H. Yang, H. Liu, B. Li, W. Luo, X. Li, W. Zhang, F. Lu, J. Fang, Y. Li, Highly efficient electron transport obtained by doping PCBM with graphdiyne in planar-heterojunction perovskite solar cells, *Nano Lett.* 15 (2015) 2756–2762.
- [58] J. Liu, T. Zhang, Z. Wang, G. Dawson, W. Chen, Simple pyrolysis of urea into graphitic carbon nitride with recyclable adsorption and photocatalytic activity, *J. Mater. Chem.* 21 (2011) 14398–14401.
- [59] B. Zhu, P. Xia, Y. Li, W. Ho, J. Yu, Fabrication and photocatalytic activity enhanced mechanism of direct Z-scheme g-C<sub>3</sub>N<sub>4</sub>/Ag<sub>2</sub>WO<sub>4</sub> photocatalyst, *Appl. Surf. Sci.* 391 (2017) 175–183.
- [60] P. Kuang, B. Zhu, Y. Li, H. Liu, J. Yu, K. Fan, Graphdiyne: a superior carbon additive to boost the activity of water oxidation catalysts, *Nanoscale Horiz.* 3 (2018) 317–326.
- [61] L. Ge, C. Han, Synthesis of MWNTs/g-C<sub>3</sub>N<sub>4</sub> composite photocatalysts with efficient visible light photocatalytic hydrogen evolution activity, *Appl. Catal. B* 117–118 (2012) 268–274.
- [62] Y. Chen, J. Li, Z. Hong, B. Shen, B. Lin, B. Gao, Origin of the enhanced visible-light photocatalytic activity of CNT modified g-C<sub>3</sub>N<sub>4</sub> for H<sub>2</sub> production, *Phys. Chem. Chem. Phys.* 16 (2014) 8106–8113.
- [63] F. He, G. Chen, Y. Yu, S. Hao, Y. Zhou, Y. Zheng, Facile approach to synthesize g-PAN/g-C<sub>3</sub>N<sub>4</sub> composites with enhanced photocatalytic H<sub>2</sub> evolution activity, *ACS Appl. Mater. Interfaces* 6 (2014) 7171–7179.
- [64] Z. Wu, H. Gao, S. Yan, Z. Zou, Synthesis of carbon black/carbon nitride intercalation compound composite for efficient hydrogen production, *Dalton Trans.* 43 (2014) 12013–12017.
- [65] Q. Xiang, J. Yu, M. Jaroniec, Preparation and enhanced visible-light photocatalytic H<sub>2</sub>-production activity of graphene/C<sub>3</sub>N<sub>4</sub> composites, *J. Phys. Chem. C* 115 (2011) 7355–7363.
- [66] Q. Xu, J. Yu, J. Zhang, J. Zhang, G. Liu, Cubic anatase TiO<sub>2</sub> nanocrystals with enhanced photocatalytic CO<sub>2</sub> reduction activity, *Chem. Commun.* 51 (2015) 7950–7953.
- [67] Z. Zhang, J. Huang, Y. Fang, M. Zhang, K. Liu, B. Dong, A nonmetal plasmonic Z-scheme photocatalyst with UV-to NIR-driven photocatalytic protons reduction, *Adv. Mater.* 29 (2017) 1606688.
- [68] Y. Yu, Y. Tang, J. Yuan, Q. Wu, W. Zheng, Y. Cao, Fabrication of N-TiO<sub>2</sub>/InBO<sub>3</sub> heterostructures with enhanced visible photocatalytic performance, *J. Phys. Chem. C* 118 (2014) 13545–13551.
- [69] M. Tabbal, T. Christidis, S. Isber, P. Mérel, M.A. El Khakani, M. Chaker, A. Amassian, L. Martinu, Correlation between the sp<sup>2</sup>-phase nanostructure and the physical properties of unhydrogenated carbon nitride, *J. Appl. Phys.* 98 (2005) 044310.
- [70] S. Lettieria, V. Gargiulob, D.K. Pallottia, G. Vitiello, P. Maddalena, M. Alfèb, R. Marotta, Evidencing opposite charge-transfer processes at TiO<sub>2</sub>/graphene-related materials interface through a combined EPR, photoluminescence and photocatalysis assessment, *Catal. Today* 315 (2018) 19–30.
- [71] Q. Liang, Z. Li, Z. Huang, F. Kang, Q. Yang, Holey graphitic carbon nitride nanosheets with carbon vacancies for highly improved photocatalytic hydrogen production, *Adv. Funct. Mater.* 25 (2015) 6885–6892.
- [72] T. Di, Q. Xu, W. Ho, H. Tang, Q. Xiang, J. Yu, Review on metal sulphide-based Z-scheme photocatalysts, *ChemCatChem* 11 (2019) 1394–1411.